Journal of Applied Fluid Mechanics, Vol. 19, No. 1, pp. 3385-3397, 2026.
Available online at www.jafmonline.net, ISSN 1735-3572, EISSN 1735-3645.
https://doi.org/10.47176/jafm.19.1.3554

Experimental and Numerical Simulation Study of Clocking Effects on Hydraulic Performance of Multi-stage Centrifugal Pump

T. Xu, B. Cui, L. Zhai†, and Z. Zhu

Zhejiang Sci-Tech University, Zhejiang Key Lab Multiflow & Fluid Machinery, Hangzhou 310018, China

†Corresponding Author Email: zhailului@zstu.edu.cn

ABSTRACT

Multistage centrifugal pumps are distinguished by their high head capacity, energy efficiency, and operational reliability. These pumps are extensively employed in boiler feedwater systems, petrochemical processing, fire protection infrastructure, and industrial process pressurization. To mitigate synchronous excitation vibrations from root imbalance, impellers are typically installed with circumferential phase differences, an approach that gives rise to the clocking effect. Hydraulic performance and transient flow patterns in the initial 3-stages of a multi-stage centrifugal pump are analyzed with respect to clocking effects at rated operating conditions. Nine clocking configurations were designed, and measurements of internal flow were conducted at three key locations within the pump. The relationships among pressure variation patterns, internal flow distribution, turbulent kinetic energy dissipation, and entropy-based energy loss were analysed. Quantitative results reveal that clocking has a notable impact on hydraulic performance, with efficiency variations of up to 14.3% at part-load and 9.1% at overload conditions. Additionally, impeller pressure fluctuations exhibited a 90° phase shift along with a principal frequency deviation of 59.17 Hz, directly linked to changes in stator–rotor interaction. These effects lead to observable improvements in internal flow behaviour. Among the nine clocking configurations, optimised impeller phase alignment reduced secondary flow structures, minimised wake-induced losses, and enhanced volumetric efficiency by up to 4.2%. These findings demonstrate that clocking optimisation is a viable strategy for enhancing flow stability and pump efficiency.

Article History

Received April 21, 2025
Revised August 6, 2025
Accepted August 22, 2025
Available online November 5, 2025

Keywords:

Clocking effect
Multistage centrifugal pumps
Pressure fluctuation
Entropy generation rate
Turbulent kinetic energy

1. INTRODUCTION

Investigating blade clocking effects presents a promising strategy for enhancing the performance of multistage centrifugal pumps. This study focuses on optimising the relative circumferential positioning between stationary guide vanes and rotating impellers in successive stages to improve overall efficiency by controlling the interference patterns between moving and stationary blade rows. Due to the continuous relative motion between these components, the internal flow in multistage pumps is inherently very unstable, leading to complex flow structures and significant pressure fluctuations resulting from rotor–stator interactions. By methodically modifying the relative angles between adjacent blade rows, blade clocking research aims to optimise the internal flow field, reduce hydraulic losses, and improve overall pump performance through favourable interference or the mitigation of adverse interference. Proper blade alignment enhances energy conversion from kinetic to energy conversion and reduces radial hydraulic loads in multistage pumps (Zhang et al., 2015) and has been shown to significantly affect the effectiveness of turbo machines. (Jahani et al., 2022).

The clocking effect (Barrio et al., 2010), first observed by Walker and Oliver (Walker & Oliver, 1972) in axial flow compressors, wake interactions from upstream blade rows impinging on downstream boundary layers have been quantitatively characterized via hot-wire anemometry. Since then, the clocking effect has been studied extensively in turbines as well. Bohn et al. (2005) examined the clocking effect in a two-stage axial flow pump using both steady-state simulations (via the frozen rotor method) and transient simulations (via the slip-grid method), comparing internal flow fields and hydraulic performance under two clocking schemes. Arnone et al. (2004) investigated how varying the circumferential relative position between consecutive vanes affects

turbine performance. Yang et al. (2015) numerically analysed the aerodynamic effects of clocking in turbomachinery, while He et al. (2015) introduced the space-time gradient (STG) method to more accurately analyse unsteady flow and blade forcing caused by clocking effects. Unlike compressors and turbines, centrifugal pumps exhibit distinct internal flow characteristics. In this context, Tan et al. (2016) quantified blade clocking effects on hydrodynamic interactions within a quintuple-stage centrifugal pump, measuring performance and vibration intensity under different clocking configurations. Their findings indicated that while the clocking effect had minimal impact on head and efficiency across the entire flow range, it significantly affected vibration behaviour. Si et al. (2024) investigated the transient hydrodynamic properties of a high-speed multistage centrifugal pump using sixteen synchronous positions. Their results showed that impeller clocking mainly impacted waveform distortion, particularly near the clearance region, where pressure fluctuations were most sensitive to the relative positions of the guide vane and impeller. The cumulative propagation of pressure fluctuations through the fluid domain was relatively minor. The least stable performance occurred when the guide vane position was fixed and the impeller was clocked at 3/4 of the maximum deflection angle. Applying the optimal clocking configuration to a prototype pump yielded a reduced vibration amplitude of 1 mm/s and an efficiency of 53.67%. Gu et al. (2019) reported that clocking positions more strongly influence the total pressure loss coefficient in circular casings with a maximum variation of 1.91%. Furthermore, Hongyu et al. (2021) explored the clocking effect in a pump as turbine (PAT) system. They investigated eight clocking schemes with angles (θ) ranging from 0° to 70° among the guide vane and volute tongue. At a flow rate of 80 m³/h, the maximum efficiency difference among the schemes was 2.45%. The configuration with $\theta = 50°$ yielded the highest efficiency for flow rates exceeding 48 m³/h. A regression model related entropy generation to total pressure loss was also developed to quantify energy losses.

It mainly influences the interstage flow dynamics in multistage centrifugal pumps, particularly the unsteady behaviour of the global main flow field. Flow losses associated with this effect are commonly evaluated using indicators such as pressure throb, turbulent kinetic energy (TKE), and entropy production. Al-Obaidi & Alhamid (2024) used the Shear Stress Transport (SST) k-ω model combined with sliding mesh technology to investigate dynamic flow patterns within a pump under varying flow rates and blade geometries. The experimental findings and their numerical simulations agreed rather well, thereby enhancing the accuracy of performance predictions. This study included a qualitative analysis of static pressure, shear stress, and velocity components, as well as a quantitative spectral analysis examining the influence of impeller blade design and operating conditions on average pressure and pressure fluctuations. These comprehensive results revealed that blade geometry significantly affects average pressure, radial, axial, and tangential shear stresses, as well as velocity magnitudes and pressure distributions. Xu et al. (2024) employed spectral decomposition via Fast Fourier Transform (FFT) to characterize hydraulic pressure transients across temporal and frequency domains. Power spectral density (PSD) was applied to extract features associated with each cavitation stage, especially the fully developed cavitation stage, which exhibited random signal characteristics. Pressure fluctuation analysis by Chen & Tan (2024) revealed dominant 169.2 Hz blade-passing-frequency (BPF) oscillations originating at the rotor-stator interface. Their Eulerian-Lagrangian framework incorporated our prior variable drag and enhanced erosion models for pumped hydro energy storage systems.

Ghorani et al. (2020) were among the first to investigate irreversible energy losses in a PAT system using the second law of thermodynamics-based entropy generation hypothesis. They simulated the three-dimensional, incompressible, steady-state flow within the PAT by solving the Reynolds-averaged Navier–Stokes (RANS) equations. Entropy generation due to both viscous dissipation and turbulence was calculated for each of the nine PAT components across a range of flow rates from 0.7 to 1.3 times the best efficiency point (QBEP). Their results revealed that turbulent entropy generation was the dominant contributor, accounting for 86.89% to 90.98% of the total entropy produced. This confirms that turbulence-induced losses are the primary source of hydraulic inefficiency in PAT systems. Sakran performed computational analysis of transient hydrodynamics in centrifugal pumps, evaluating performance variations across differential blade configurations. The results showed that increasing the number of blades improved hydraulic performance, raising both power of the shaft and head. The impeller with seven blades achieved the highest efficiency at 78.7%, which was 0.27% greater than that of the original type. Additionally, pressure fluctuation amplitudes decreased with more blades; the lowest amplitude (4960.79 Pa) was observed for the impeller with nine blades. To better understand energy loss mechanisms during transient multiphase flow, Wang et al. (2020) recommended using numerical simulations and visualisation techniques in rotodynamic pumps. Their approach incorporated interphase pressures and bubble diameters to more accurately model transitions in flow regimes. Complementary to this, imaging experiments and transient numerical simulations were proposed to examine multiphase interaction and flow instability. Fonseca et al. (2024) conducted time-resolved, two-dimensional PIV experiments precisely phase-locked to the impeller rotation angle. Research outcomes revealed 34% discharge flow modulation at the volute nozzle during blade rotation, maintaining 2.2% upper-bound experimental uncertainty. Similarly, An average hydrodynamic deviation of 33.5% was observed in inter-blade passage flow fields. Perissinotto et al. (2024) established an energy dissipation framework for P23 radial impellers in hydraulic operation, deriving a predictive head correlation that quantifies recirculation, shock/incidence, and frictional losses. Quantitative evaluation was according to experimental PIV data, providing insights into wall shear stress and velocity vector fields, both of which are useful for head loss assessment. Chen et al. (2023) and Luo et al. (2024)

presented comprehensive numerical studies on energy transfer and dissipation in centrifugal pump impellers. This research elucidates impeller-specific dissipation mechanisms while quantifying energy transfer efficiency within hydraulic pathways.

Despite extensive research on the clocking effect in compressors or turbines, its impact in centrifugal pumps has received comparatively little attention. (Maestre Di Cioccio et al., 2024), especially concerning pressure fluctuations and transient radial forces. Most existing studies focus on two-stage blade row configurations, which failed to account for downstream-fluid-induced perturbations affecting upstream vane aerodynamics, while study on the clocking effect remains insufficient. To address this gap, it is necessary to investigate multistage configurations with more than two stages. This study is structured as: Section 2 delineates computational methodologies, Section 3 examines hydrodynamic simulation outcomes, and Section 4 synthesizes conclusive findings.

2. NUMERCIAL MODEL AND METHOD

2.1 Model Structure and Numerical Simulation

A 10-stage centrifugal pump configuration was geometrically defined within the NX environment, establishing the computational domain for subsequent analysis, and meshing was performed using ICEM to discretise the flow field for numerical analysis. Figure 1 depicts the whole model. To strike a balance between processing expense and practicality, the research focuses on the clocking effect within the first three impeller stages. These stages were individually extracted to construct a new set of clocking configurations for detailed evaluation. Primary hydraulic elements of the multistage centrifugal pump comprise the suction manifold, impeller, stationary diffuser system, and discharge volute assembly. The pump is designed for a flow rate of Q_d=290 m^3/h, a head delivery of H=2369 m, and a rotational velocity of n=3550 rpm. Critical geometrical characteristics of principal components are tabulated in Table 1.

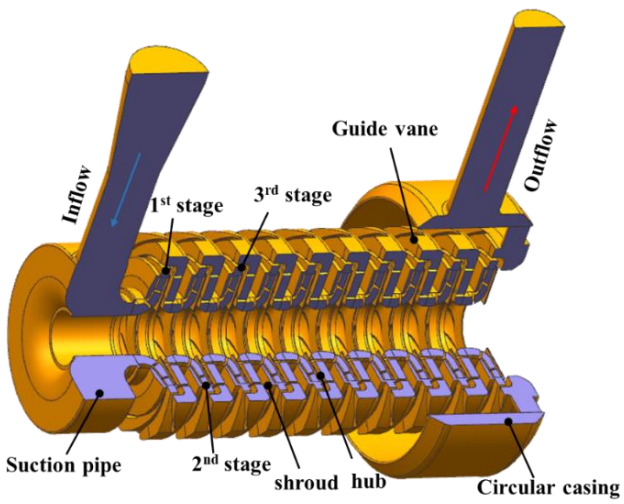

Fig. 1 Multistage pump model

Table 1 Geometric parameters of main components of model pump

Impeller parameter	Impeller		
	First	Second	Final
Impeller inlet diameter, mm	200	196	196
Impeller outlet diameter, mm	362	362	362
Number of blades	7	7	7
Blade outlet angle, °	20	20	20
Impeller outlet width, mm	17	17	17

The grid for the complete flow field of the multistage pump was generated using ICEM. A high-quality structures mesh was applied to critical components, including the inlet, outlet, shroud, hub, and impellers, to enhance solution convergence. To improve calculation accuracy, boundary layer refinement and wall grid densification were implemented for each component. The accuracy and stability of the simulation are highly dependent on the wall mesh specifications, particularly for key low components such as guide vanes and impellers, as indicated by the dimensionless wall distance, y^+. The boundary layer mesh for the impeller consists of 15 inflation layers, with a growth rate of 1.2 and a first-layer thickness of 0.03 mm. The resulting y^+ values are approximately 48 for the impeller and 67 for the guide vane. These values fall within the range suitable for applying standard wall functions in turbulence modelling.

Grid independence of the computational model was verified, and Fig. 2(b) displays the whole flow field mesh. Six different mesh sets were tested under design flow conditions. The first three sets produced head coefficient errors of 1.1%, 0.8%, and 0.5%, respectively. In contrast, the fourth and fifth sets yielded errors below 0.07%, indicating convergence. The results stabilised with the fifth and sixth mesh sets, confirming grid independence. The solution domain was discretized into 9,108,640 control volumes to satisfy competing accuracy and resource constraints. Fig. 2(b) illustrates the grid independence verification process.

The steady and unsteady flow fields of the multistage pump were simulated using CFX, based on the standard $k-\varepsilon$ model. The governing equations for the model are as follows:

$$\frac{\partial(\rho k)}{\partial t}+\frac{\partial(\rho u_j k)}{\partial x_j}=\frac{\partial}{\partial x_j}[(\mu+\frac{\mu_t}{\sigma_k})\frac{\partial k}{\partial x_j}]+P_k-\rho\grave{o} \quad (1)$$

$$\frac{\partial(\rho\grave{o})}{\partial_t}+\frac{\partial(\rho u_j\grave{o})}{\partial x_j}=\frac{\partial}{\partial x_j}[(\mu+\frac{\mu_t}{\sigma_{\grave{o}}})\frac{\partial_{\grave{o}}}{\partial x_j}]+C_{\grave{o}1}\frac{\grave{o}}{k}P_k-C_{\grave{o}2}\rho\frac{\grave{o}^2}{k} \quad (2)$$

Among them, C_μ=0.09 is the turbulent viscosity coefficient, $C_{\varepsilon1}$=1.44 is the coefficient of the equation generation term, $C_{\varepsilon2}$=1.92 is the coefficient of the equation dissipation term, σ_k=1.0 is the Prandtl number, and σ_ε=1.3 is the Prandtl number.

For the steady simulations, a frozen rotor interface was applied between adjacent stationary and rotating domains.

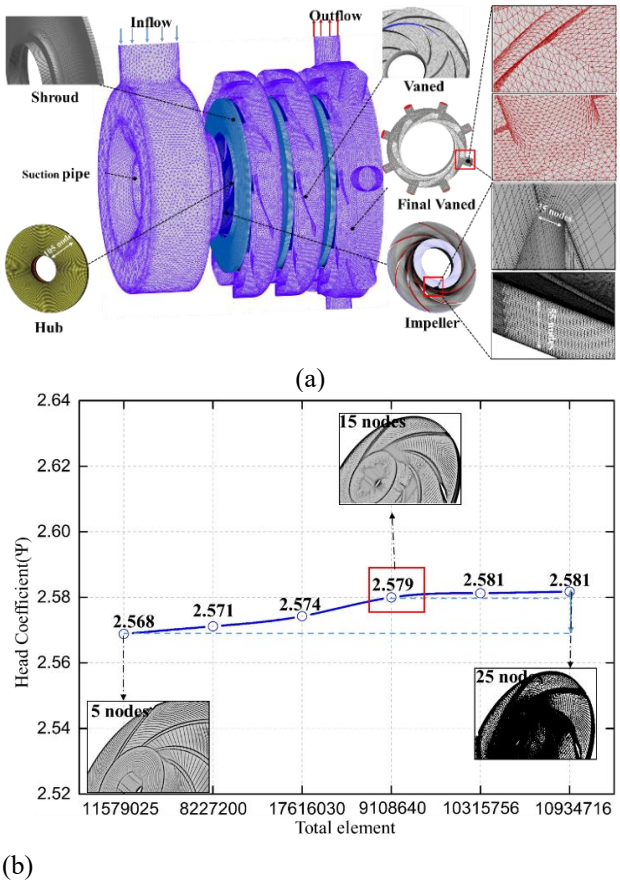

Fig. 2 Full-field meshing and independence: (a) mesh (b) mesh independence

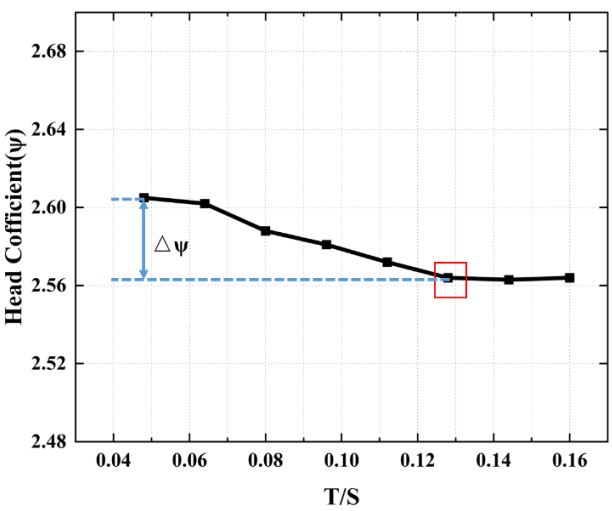

Fig. 3 Time independence verification

For transient simulations, a rotor–stator interface with moving mesh (transient rotor–stator interaction) was employed. The computational domain employed stagnation pressure boundary conditions at the inlet (referenced to 1 atm absolute pressure), with hydrodynamic outflow regulated through specified mass flux at the discharge. The working fluid was water, with a density of 1000 kg/m^3, a specific volume of 4.2×10^3 J/kg, and a temperature of 25 °C. Based on the geometric and flow parameters of the model, the reference mass flow rate was calculated to be 128.88 kg/s.

For the unsteady calculation, the SIMPLEC algorithm was adopted to enhance convergence by improving the pressure correction equation. The convective terms were discretised using a second-order high-resolution scheme. Convergence was evaluated using the root-mean-square (RMS) residuals, with a threshold of 10^{-5}. To ensure the simulation results were time-independent, the total duration was carefully selected to eliminate the impact of the computation time on the numerical simulation outcomes. Figure 3 presents the variation of the pump's head coefficient over time. It shows significant fluctuations during the initial stage, which gradually stabilise, indicating that the internal flow field has reached a quasi-steady state. Considering computational cost and efficiency, a total simulation time of 0.1305 s was chosen, corresponding to 8 full impeller revolutions. The value of the time step △t was 1.4084×10^{-4} s, allowing for an impeller rotation of 3° per time step, over 960 steps in total.

2.2 Clocking Scheme Design

Multistage centrifugal pumps exhibit extensive combinatorial diversity in clocking configurations due to stage multiplicity and variable impeller angular indexing. In this study, the methodology establishes the first-stage impeller azimuthal orientation as the datum position (θ=0°). Downstream impellers (Stages 2-3) undergo controlled angular displacement to generate discrete phase configurations. The second-stage impeller's rotation angle is represented by θ_1, as seen in Fig. 4(a). while that of the final-stage impeller is θ_2. Each impeller in the pump consists of seven blades with identical geometric parameters. The angular spacing between two adjacent blades is 48°, and the maximum stagger angle between the impellers is therefore limited to half of this blade-to-blade angle, i.e., 24°. Fig. 4(b) shows the locations of monitoring points placed at the outlets of impellers that are subject to significant dynamic and static interventions. Monitoring Points A、C are situated at the pressure-side discharge edges of opposing impeller blades, whereas Point B resides at the meridional midpoint of the inter-blade flow channel. Designated as the P-plane and visually identified (yellow), this reference surface enables quantitative analysis of outlet static pressure distributions.

Based on insights from similar studies and to support the development of an empirical model, Computational tractability dictated investigation of nine discrete phase offsets (6° increments from 0° to 24°), optimizing the accuracy-resource equilibrium. The baseline configuration, denoted as PL1, represents the initial clocking scheme in which the circumferential angle of the impellers remains unaltered across all stages. In configurations PL2 to PL6, the second-stage impeller is held at a constant clocking angle of 24°, while the final-stage impeller is incrementally rotated by 6° intervals to create variation. Configurations PL7 to PL9 implement a synchronous change in the final-stage impeller's clocking angle, also in 6° intervals. The specific impeller configurations are illustrated in Table 2.

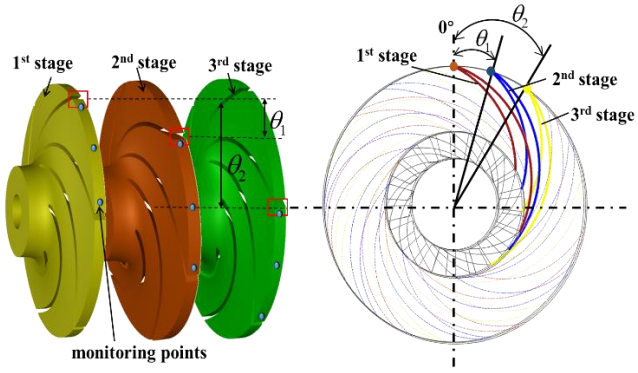

(a)

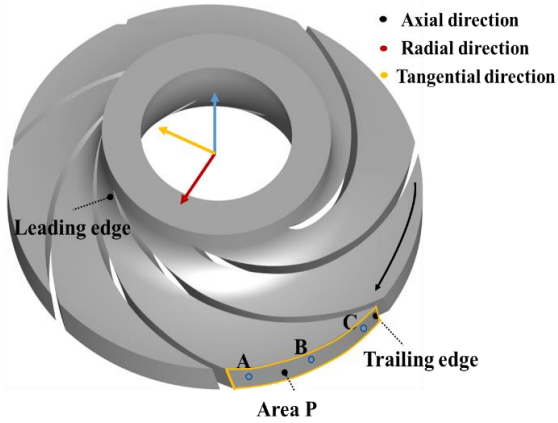

(b)

Fig. 4 Clocking of impeller scheme (a), Monitoring point indication (b)

Table 2 Angle variation of impeller clocking

Scheme	First impeller[°]	Second impeller(θ_1) [°]	Final impeller(θ_2) [°]
PL1	0	0	0
PL2	0	24	0
PL3	0	24	6
PL4	0	24	12
PL5	0	24	18
PL6	0	24	24
PL7	0	6	12
PL8	0	12	18
PL9	0	18	24

3. Analysis Of Results

3.1 Analysis of Experimental Characteristic and Numerical

The 0217-P-102B hydrogenation feed pump underwent external performance validation at Ebara Great Pumps Co., Ltd.'s accredited test facility, establishing baseline hydraulic characteristics for this multistage configuration. The tests were carried out in accordance with the standardised procedures specified by International Organization for Standardization (ISO). The facility is equipped with internationally recognised test software that complies with various global testing standards. Fig. 5(b) depicts the experimental setup primarily consists of a water tank, variable frequency motor, control valves, sensors, flowmeter, pump, and data acquisition system. The Jiamusi-made variable frequency

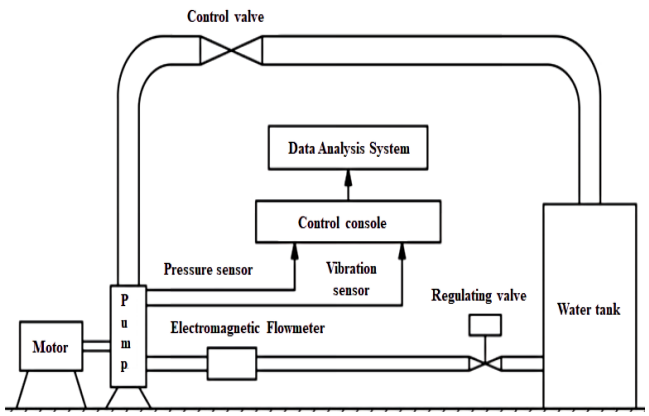

(a)

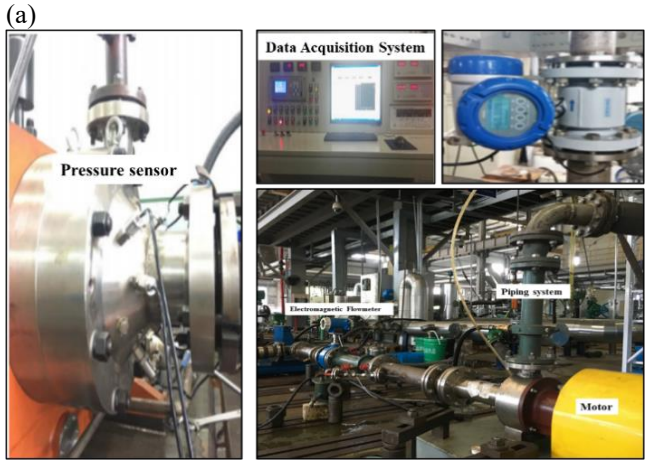

(b)

Fig. 5 Experimental system: (a) schematic (b) photographic views

motor rotates at a speed of 1494 min^{-1} and has a rated voltage of 10,000 V. To measure the static inlet and outlet pressures, a DN300 pressure sensor was employed, with operational ranges of -0.1–5 MPa for negative pressure and 0–10.6 MPa for positive pressure. The sensor has an accuracy rating of 0.2 grade. An electromagnetic flowmeter was installed on the outlet pipeline to measure the flow rate. While the flowmeter itself supports a range of 35–350 m^3/h, the actual experimental pipeline range used was 3–75 m^3/h.

Computational-experimental divergence in Fig. 6 reveals consistent simulation overprediction, principally stemming from neglected mechanical loss mechanisms in the numerical model. However, the overall trend between the two is consistent, and the deviation remains within acceptable engineering margins. As the flow rate increases, both the simulated and experimental head values gradually decrease, with a 2.4% maximum head inaccuracy. The head-flow curve demonstrates a monotonically decreasing trend with no occurrence of a hump, indicating that the pump operates reliably and stably across the entire flow range. The efficiency curves obtained from simulation and experiment both show a rise followed by a decline consistent with typical pump behaviour. The maximum efficiency error between the two datasets is 6.4%. Additionally, a comparison between simulated and experimentally measured pressure fluctuations shows that while the overall fluctuation pattern agrees well, the experimentally measured pressure

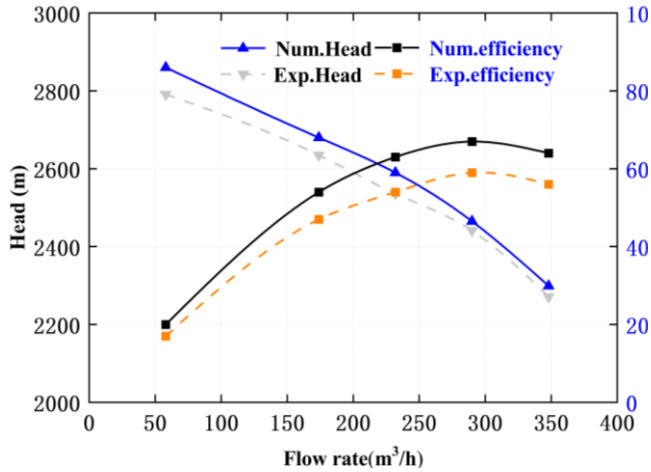

(a)

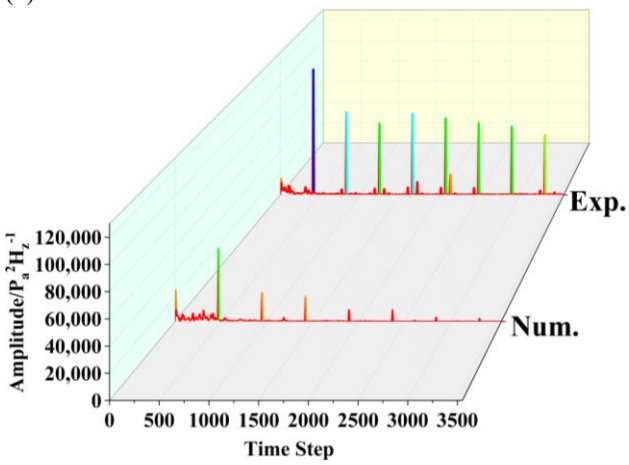

(b)

Fig. 6 Comparison of experimental and numerical simulation head efficiency (a) Frequency domain comparison (b)

peaks are slightly higher. The average error in pressure amplitude is 4.1%, with a maximum deviation of 7.8% at the peak. Experimental computational alignment confirms the selected turbulence closure and numerical framework reliably resolve clocking effect modulation of unsteady flow structures in multistage pump configurations.

3.2 Analysis of Pressure Fluctuation

Based on both experimental data and numerical simulations, the clocking effect of the first three-stage impeller of the multistage pump was investigated using a discrete modelling approach. Fig. 7 reveals the variation in head coefficient and hydraulic efficiency across distinct clocking configurations. The head coefficient is a key dimensionless parameter that quantifies the effectiveness of converting the fluid's kinetic energy into pressure energy. It offers a theoretical foundation for turbomachinery design, performance assessment, and optimization. The head coefficient is defined as:

$$\Psi = \frac{2gH}{u_2^{\ 2}} \tag{3}$$

where, u_2 is the impeller outlet circumferential velocity, H is the centrifugal pump head, g is the acceleration of gravity.

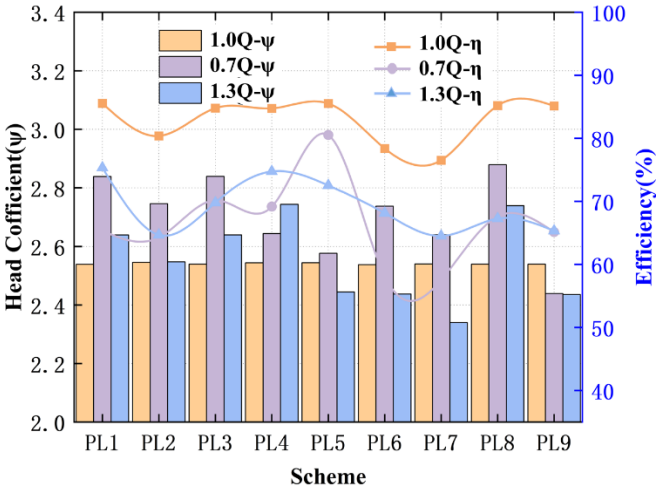

Fig. 7 Comparison of head coefficients and efficiency of each scheme

A comparative analysis of the clocking scheme PL1–PL8 reveals notable sensitivity in hydraulic performance under off-design conditions. At part-load (0.7Q), the head coefficient exhibits a maximum variation of Δψ=15.2%, reaching a peak value of ψ=2.88 under configuration PL8. Under overload conditions (1.3Q), the fluctuation is Δψ=14.9%, with a maximum value of ψ=2.74 at PL4. By contrast, at the design point (1.0Q), the head coefficient remains relatively stable, ranging from ψ=2.53 to 2.54, with an average of ψ=2.54. Similarly, hydraulic efficiency demonstrates significant variation under non-design conditions: a maximum deviation of 14.3% and 9.1% at 0.7Q and 1.3Q, respectively. At the design point, however, efficiency remains stable in the range of η=75%–85%. These findings clearly indicate that impeller clocking has a pronounced influence on multistage pump hydraulic performance, particularly at extreme operating regimes. The results underscore the importance of a systematic investigation into stator–rotor phase interactions for targeted optimisation.

A more thorough examination of the impeller's internal flow characteristics and pressure distribution was carried out because of the notable effect that clocking has on head efficiency. The pressure fluctuation characteristics under various clocking configurations were examined in the frequency and temporal domains, introducing the pressure fluctuation coefficient C_p as a quantitative indicator. Fig. 8 presents the variation of C_p across different clocking schemes, with the ordinate representing C_p and the abscissa denoting the simulation time step. The pressure fluctuation coefficient is defined as follows:

$$C_p = \frac{p - p_\infty}{0.5\rho u_2^2} \tag{4}$$

$$u_2 = \frac{n\pi D_2}{60} \tag{5}$$

where, P represents the fluid's local pressure at a specific location, and P_∞ is the static pressure of the incoming flow (i.e., the pressure far away from the object or disturbance area). u_2 and D_2 stand for the circumferential velocity and diameter of the impeller output, respectively, while ρ is the

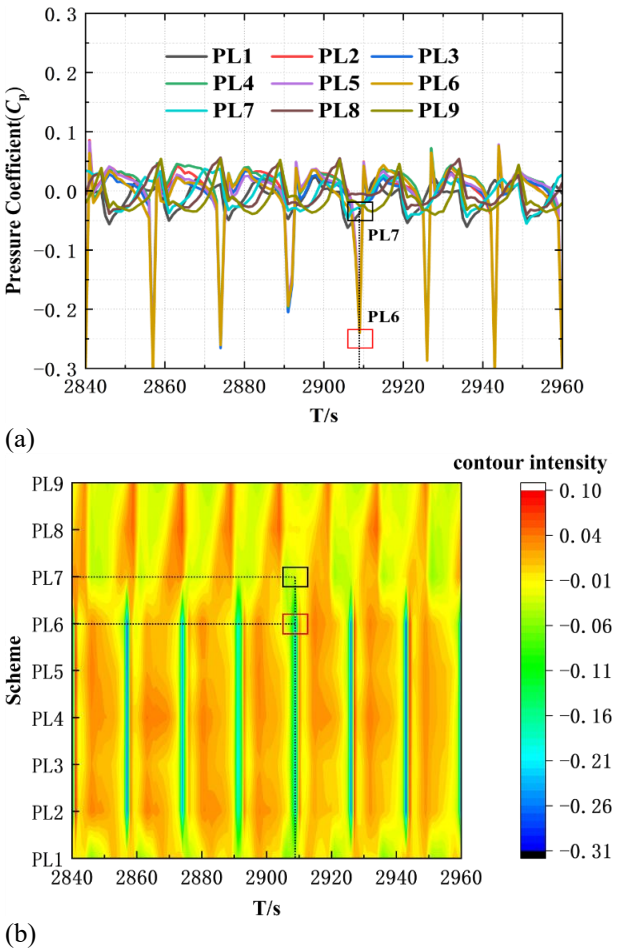

Fig. 8 Monitoring of the pressure coefficient fluctuation (a) and contour intensity (b) of the second impeller

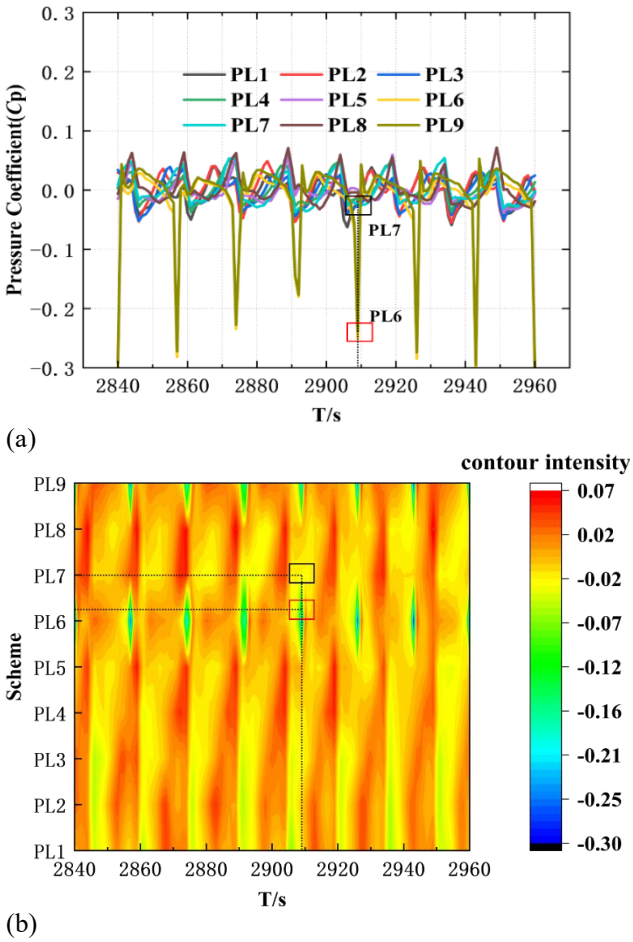

Fig. 9 Monitoring of the pressure coefficient fluctuation (a) and contour intensity (b) of the final impeller

density of the liquid medium.

In the time-domain analysis, fluctuations at the impeller outlet exhibit seven distinct peaks and troughs per cycle, corresponding to the number of impeller blades, indicating a clear periodic oscillation driven by blade-passing frequency. Across clocking configurations PL1–PL6, the pressure fluctuation coefficient C_p ranges from -0.3 to 0.09, with a total fluctuation amplitude of 0.39. Notably, configuration PL6 shows the largest amplitude, attributed to its complex flow structures and stronger interference effects from upstream impeller flow. Further insight is provided by the contour intensity plots, where the ordinate denotes various time series schemes and the abscissa represents flow time. These contours reveal pronounced differences in pressure fluctuation behaviour across clocking schemes.

In PL2 to PL6, significant pressure amplitude variations occur at the blade-passing frequency, suggesting strong rotor–stator interaction. Conversely, PL1 to PL9 generally exhibit more stable pressure variations. Additionally, a 90° shift is observed between the pressure waveforms of the 24° (PL2) and 0° (PL1) clocking schemes. Specifically, when PL1 is at its minimum pressure point, PL2 reaches its maximum, highlighting a strong phase-dependent influence of clocking angle on unsteady pressure behaviour.

The pressure fluctuation characteristics in the final-stage impeller area are shown in Fig. 9. At a normalised time of 0.35, the pressure fluctuation amplitude is observed to be approximately 8% lower than the second-stage impeller outlet. The pressure fluctuation coefficient in this region ranges from -0.3 to 0.05. A key observation is the nonlinear amplification effect in the energy transfer across the interstage flow field. This is most clearly demonstrated by the substantial change in fluctuation amplitude between PL6 at the second-stage impeller and PL9 at the final-stage impeller, where the fluctuation amplitude increases by a factor of 2.9 compared to the second-stage impeller. These results indicate that the clocking effect exhibits spatial selectivity in influencing pressure fluctuation. Specifically, intra-stage flow modulation is significant, and clocking optimisation can reconstruct the wake-potential flow coupling mechanism within the impeller channel, leading to fluctuation amplitude variations of 35%–40%. In contrast, inter-stage interference is relatively weak. Adjusting the clocking angle has minimal influence on the propagation intensity of pressure fluctuations between stages.

The study given above shows that the clocking effect enhances the flow condition at the impeller outlet. delays the onset of the "hump area" in the head-flow curve, and partially reduces pressure fluctuations. Specifically, clocking induces a circumferential phase shift in the

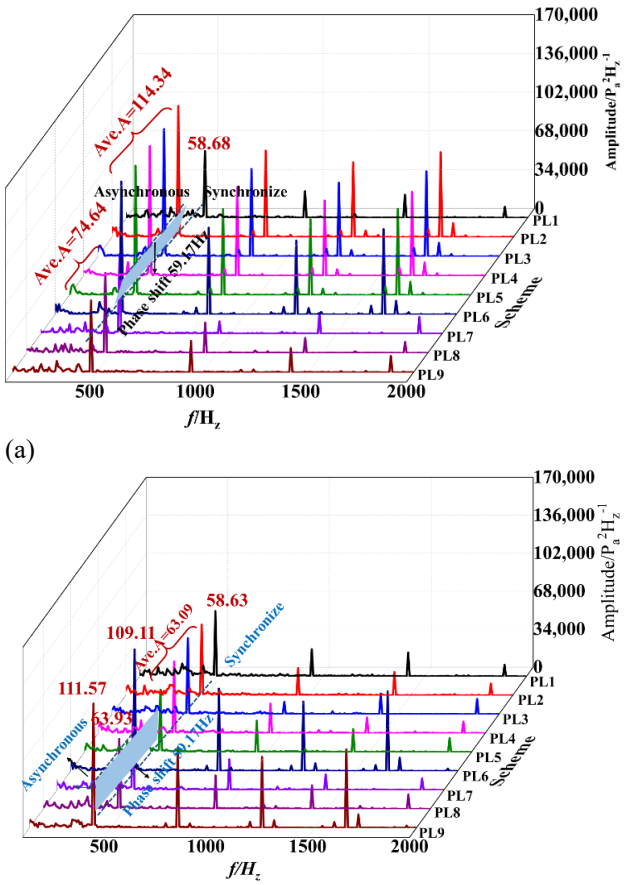

Fig. 10 Frequency of impeller: (a) second, (b) final

downstream-stage impeller while the upstream impeller maintains a constant pressure. This mostly affects the magnitude of pressure variations by creating a hysteretic effect in the outlet pressure peak of the downstream impeller, indicating the presence of a phase shift in the pulse waveform.

To further analyse the fluid pressure variation and phase shift laws, FFT is applied to extract amplitude-frequency characteristics. Fig. 10 illustrates the frequency domain pressure signature at the second-stage impeller discharge (Point B). Fig. 10(a) indicates that the primary frequency of PL2–PL6 is 414.16 Hz, with the blade passing frequency representing the dominant frequency and a discernible component that pulses at a high frequency. PL1's primary frequency amplitude is around 58.63×10³ Pa²Hz^{-1}, whereas the amplitudes of PL2–PL6 average around 114×10³ Pa²Hz$^{-1,}$ which is 11.9 times higher. For PL7–PL9, the dominant frequency shifts to 473.33 Hz, with an average amplitude of 74×10³ Pa²Hz^{-1}, representing a 26.2% increase compared to PL1. A frequency lag of 59.17 Hz is observed between the asynchronous and synchronous clocking schemes, indicating a substantial phase deviation. Pressure fluctuations at Stage 2 impeller outlet exhibit equivalent spectral energy at f_r, 2fBPF (frequency band pass filter) and 3fBPF, confirming harmonic equivalence in blade-passing excitations.

Figure 10(b) further illustrates variations in the frequency domain for the second impeller. Between PL2 and PL5, the average main frequency amplitude is 63.09×10³ Pa²Hz^{-1}, which is about 7.6% more than that of PL1. Configurations PL6 and PL9 show the most significant increase, reaching 109.11×10³ Pa²Hz^{-1} and 111.57×10³ Pa²Hz^{-1}, respectively, an increase of 88.2% compared to PL1. This phenomenon may be attributed to the circumferential alteration of the upstream impeller's clocking effect, which causes the outflow fluid velocity loop to rise. The leaf inlet fluid's energy and flow state are influenced by intricate interactions and exchanges.

The blade passing frequency of 414.16 Hz exerts the most significant effect on pressure pulsations within the impeller. The blade transduction theory is derived from equation (6):

$$f = \frac{n}{60} \cdot l = 414.47\text{Hz} \tag{6}$$

where n and l represent for pump's rotational speed and blade count, respectively.

3.3 Analysis of Impeller Outlet Pressure

A thorough examination of this research, encompassing dominant frequency amplitude spectra, phase shift characteristics, pressure fluctuation behaviour in the frequency domain, and overall hydraulic performance, identifies PL5 as the optimal configuration. It achieves superior head efficiency, accompanied by pronounced periodicity in pressure fluctuations. In contrast, configurations PL2 and PL8 exhibit reduced hydraulic efficiency and notable phase drift, distinguishing them as performance extremes. This stratification establishes PL2, PL5, and PL8 as critical benchmark configurations for subsequent vorticity-resolved analysis of clocking-induced stator–rotor interaction mechanisms governing multistage pump internal flow physics.

To further explore the influence of clocking, this study examines the correlation between the main frequency amplitude and static pressure distribution at the second-stage impeller outlet. According to Fig. 11, the main frequency amplitude varies approximately proportionally to static pressure along the impeller blade channel. A progressive adverse pressure gradient develops across the blade passage, transitioning from suction-surface flow detachment zones to pressure-surface stagnation regions, with localised peaks occurring near the blade edges. The outflow region exhibits substantial static pressure instability ($\Delta P/P_{ave}$=9.68%) with a time-averaged pressure of 3510 kPa, reflecting limits on energy conversion efficiency.

Consequently, PL1 exhibits attenuated pressure fluctuation amplitudes with clear periodicity, in contrast to the significant pulsations observed in other configurations. These intensified fluctuations are primarily attributed to steep static pressure gradients near the impeller discharge rim. Such gradients give rise to progressive low-pressure zones, particularly evident in PL8, which displays pronounced depression across clocking angles 6°–24°, suggesting a potential for vapour core formation and incipient cavitation. Conversely, PL2 develops localised

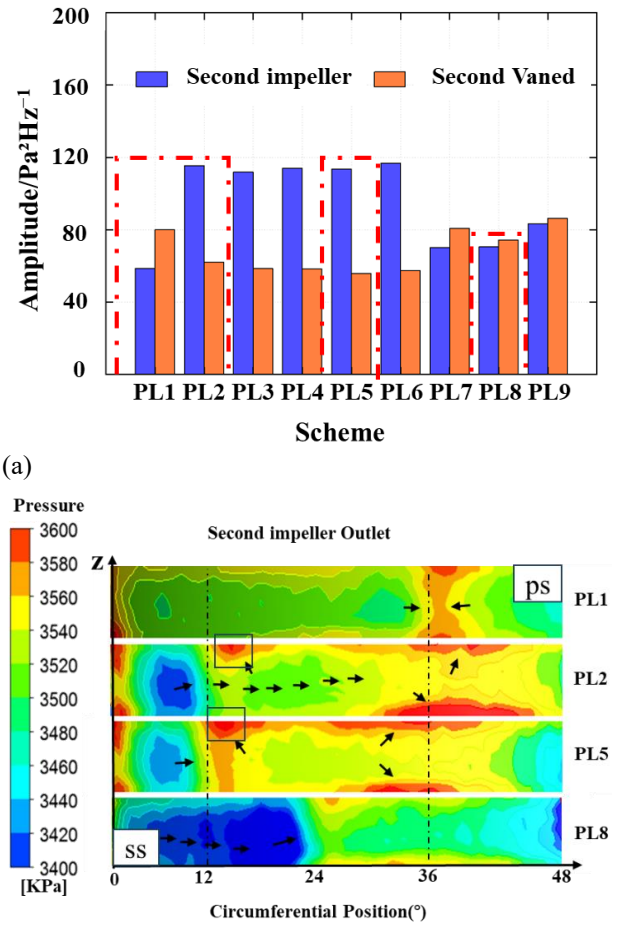

Fig. 11 Main frequency amplitude and static pressure variation of the second impeller

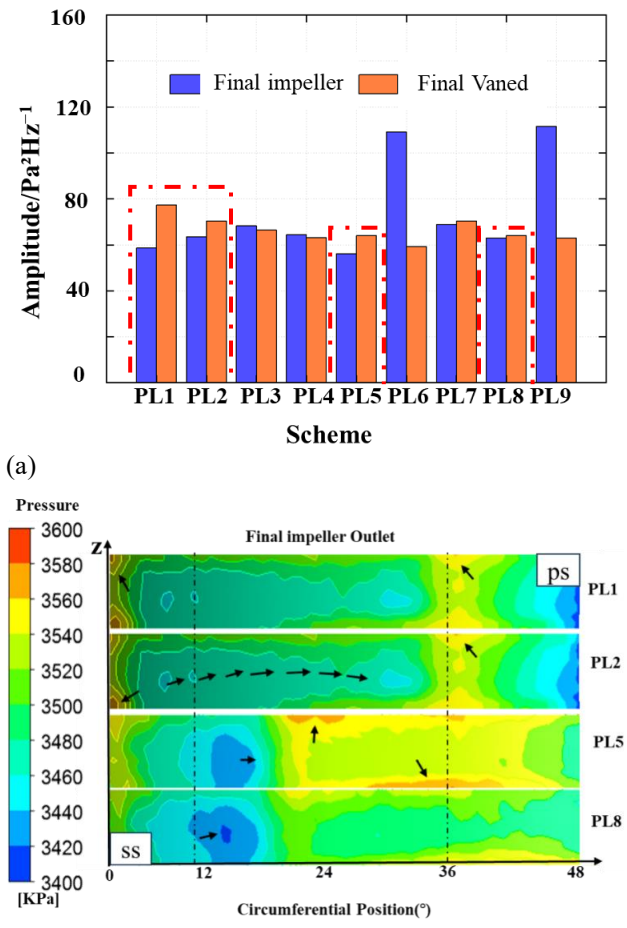

Fig. 12 Main frequency amplitude and static pressure variation of the final impeller

high-pressure concentrations around the 36° discharge position, primarily due to discharge jet impingement.

The fluid initially accumulates along the pressure surface of the impeller's upper half, driven by the substantial blade thickness at the hub-side leading edge. Modifications in the flow field state and pressure distribution at the impeller outlet, induced by clocking adjustments, result in abrupt shifts in flow direction, leading to a rapid increase in velocity and turning intensity. These circumstances encourage the emergence of unstable flow patterns, including separation zones, reflux, and second flow. which collectively exacerbate flow instability within the impeller passage.

The pressure distribution properties at the outflow region of the final-stage impeller are shown in Fig. 12. Compared to the second-stage impeller, the coefficient of isobar spacing variation is significantly lower, and the pressure gradient exhibits a highly ordered, axisymmetric pattern, indicating a smooth and gradual rise in pressure. Notably, the presence of local high-pressure jump points is eliminated due to the formation of a low-momentum-loss potential flow core region. This structural improvement reduces the system's susceptibility to upstream disturbances by approximately 40%, thereby enhancing both flow stability and anti-disturbance toughness. The primary mechanism behind this stabilisation is the strong interaction between potential flow and wake structures. The reconstruction of the dynamic and static vortex system shows that the clocking impact dramatically alters the pressure distribution in the secondary impeller zone. However, the time change only results in mild pressure reconstruction at the final impeller's output since the flow is completely developed and there is no stator restriction downstream.

3.4 Analysis of Blade-to-Blade Entropy Generation

The analysis of inlet and outlet pressure fluctuations provides critical insights into the internal flow dynamics, while the rate of entropy generation serves as a key metric for assessing energy losses in fluid machinery. During the energy conversion process, entropy generation is unavoidable; however, it can be effectively used to analyse and quantify internal flow losses. In turbulent flows, the total entropy generation of a fluid particle can be decomposed into two main components: the entropy generation due to mean flow motion (time-averaged behaviour) and the entropy generation caused by velocity fluctuation. The following formula is used for calculation:

$$\dot{S}_{D'''} = \dot{\bar{S}}_{D'''} + \dot{S}_{D'''} \tag{7}$$

$$\dot{S}_{\bar{D}}''' = \frac{\mu}{T}\{2[(\frac{\partial \bar{u}}{\partial_x})^2 + (\frac{\partial \bar{v}}{\partial_y})^2 + (\frac{\partial \bar{w}}{\partial_z})^2] + [(\frac{\partial \bar{v}}{\partial_x} + \frac{\partial \bar{u}}{\partial_y})^2 + (\frac{\partial \bar{w}}{\partial_x} + \frac{\partial \bar{u}}{\partial_z})^2 + (\frac{\partial \bar{v}}{\partial_z} + \frac{\partial \bar{w}}{\partial_y})^2]\} \tag{8}$$

$$\dot{S}_{D'}''' = \frac{\mu}{T}\{2[(\frac{\partial u'}{\partial_x})^2 + (\frac{\partial v'}{\partial_y})^2 + (\frac{\partial w'}{\partial_z})^2] + [(\frac{\partial v'}{\partial_x} + \frac{\partial u'}{\partial_y})^2 + (\frac{\partial w'}{\partial_x} + \frac{\partial u'}{\partial_z})^2 + (\frac{\partial v'}{\partial_z} + \frac{\partial w'}{\partial_y})^2]\} \tag{9}$$

Based on Herwig's suggested methodology (Herwig, 2010; Kock & Herwig, 2005), the entropy generation by velocity fluctuation can be calculated by the formula:

$$\dot{S}_{D'}''' = \frac{\rho\varepsilon}{T} \tag{10}$$

where ρ denotes the fluid density and ε denotes the turbulent dissipation rate.

Based on the aforementioned calculations, the examination of entropy generation in various places may be used to investigate the distribution of internal flow loss.

As illustrated in Fig. 13, a strong correlation is observed between the TKE dissipation and the entropy generation rate (EGR) distributions at span=0.5 across all investigated clocking schemes. Each configuration exhibits a similar spatial pattern: low TKE values are seen close to the vane outlet and impeller intake. whereas high TKE regions (highlighted in red) concentrate near the impeller outlet and certain inlet zones. In all clocking configurations, the maximum TKE consistently localises at the impeller discharge for all schemes. Quantitative analysis reveals that clocking angle significantly affects the minimum TKE values: PL1 attains the highest minimum TKE (1.37 m²/s²). PL2 and PL8 exhibit intermediate minima of 1.23 m²/s² and 0.996 m²/s², respectively. PL5 achieves the lowest TKE, at 0.943 m²/s², indicating that optimised clocking can effectively suppress turbulence intensity. A blade-to-blade analysis further reveals an asymmetry in TKE distribution. The pressure surfaces consistently exhibit weaker TKE than the suction surfaces. This asymmetry arises from rotational-induced vortex shedding along the suction side, which enhances local turbulent production. Notably, the spatial distribution of TKE dissipation exhibits strong congruence with EGR patterns.

When viscous dissipation is neglected, turbulent fluctuation dissipation becomes the dominant entropy generation mechanism within the pump. Contributions from the trailing edge to the EGR are negligible. Quantitative analysis shows that schemes PL1 and PL2 reach peak EGR values of approximately 2×10⁴ W/m³/K, which average EGR across the flow domain is around 2000 W/m³/K. The leading edge of the blades is where the greatest amount of entropy is constantly generated. where complex interactions between the inflow and rotating blade surfaces intensify thermodynamic irreversibility. Elevated EGR values are also observed near blade walls along the primary flow direction, correlating with complex inlet flow structures under rotational effects. As the impeller undergoes temporal and spatial evolution, clocking-induced variations in fluid impact angle fundamentally alter the energy transfer mechanisms. Consequently, significant energy losses arise

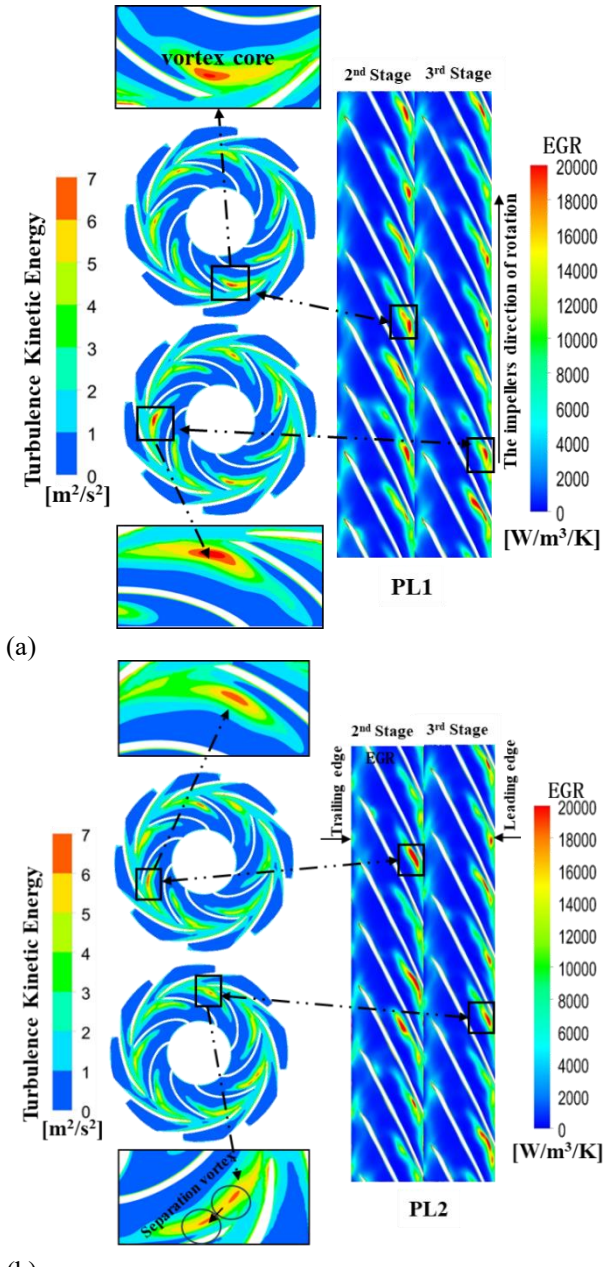

Fig. 13 Turbulent kinetic energy dissipation and entropy production rate of the impeller of schemes PL1(a)、PL2(b)

from complex flow phenomena, including leading edge fluid impact, trailing edge wake interactions, and flow separation-induced vortices. These mechanisms collectively dominate dissipation in high EGR regions.

Figure 14 indicates that configuration PL8 exhibits a high EGR at the blade leading edge, accompanied by an extensive high-loss region and a pronounced entropy generation zone near the inlet hub. This distribution highlights the significant influence of impeller clocking

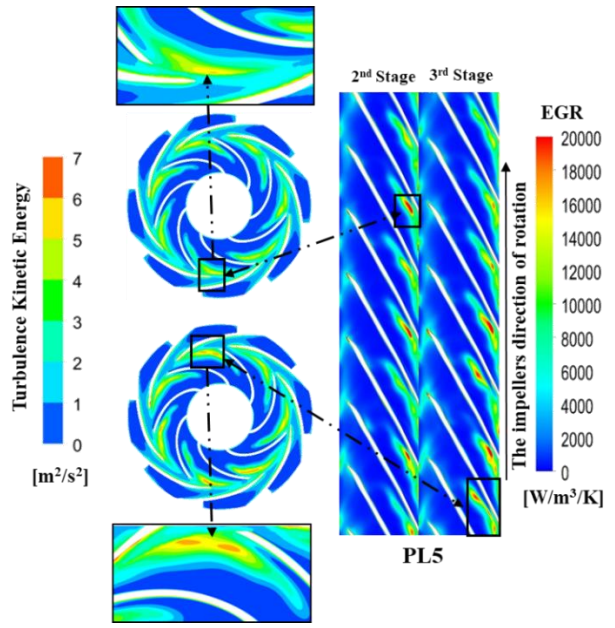

(a)

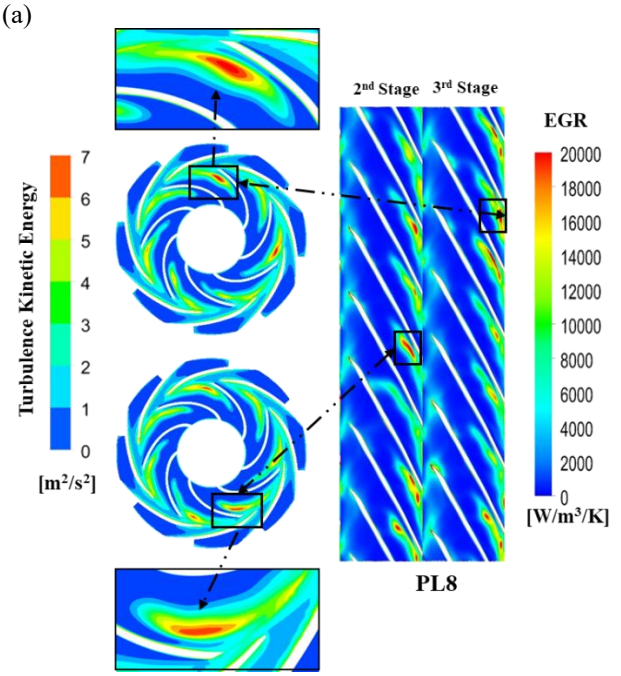

(b)

Fig. 14 Turbulent kinetic energy dissipation and entropy production rate of the impeller of scheme PL5(a)、PL8(b)

position on internal loss mechanisms, indicating that PL8 is suboptimal in terms of flow efficiency. The results confirm that the clocking effect fundamentally reshapes the internal flow field structure by modifying stator–rotor interaction. These perturbations disrupt the designed energy transfer processes, leading to flow separation and the emergence of secondary flows, which in turn generate increased local entropy. In contrast, the blade leading edge in configuration PL5 exhibits the least amount of entropy generation. indicative of a well-attached flow and significantly reduced loss levels. These findings underscore that strategic variation of the impeller clocking angle presents a viable pathway for aerodynamic loss reduction and performance optimisation.

4. CONCLUSION

Based on numerical simulations using the standard $k-\varepsilon$ model, in this study, a multistage centrifugal pump's clocking effect is examined. The key findings are summarised as follows:

(1) Clocking angles between impellers significantly influence multistage centrifugal pump hydraulic characteristics, especially under off-design conditions. At part-load (0.7Q) and overload (1.3Q), efficiency fluctuates by up to 14.3% and 9.1%, respectively, while head coefficient variations exceed 14%. Conversely, performance at the design point operation (1.0Q) remains relatively stable. These variations originate from altered stator–rotor interactions, suggesting that optimal clocking configurations differ depending on performance targets, whether maximising head or efficiency.

(2) Clocking angle changes between upstream and downstream impellers induce phase shifts in pressure pulsations, leading to either lead or lag of pressure peaks. Spectral analysis reveals a maximum phase shift of 90° occurring at 58.17 Hz, representing the peak angular displacement between excitation and response frequencies. emphasising the need to control impeller alignment to mitigate unsteady flow effects.

(3) Positioning of the impellers has a notable impact on the EGR and TKE of the model pump. The region along the mainstream direction, close to the blade wall, shows a higher EGR and TKE, which exacerbate the flow's irregularity and the advancing LEGR. Further, the TKE region of 0.943 m²/s² is diminished.

(4) In the PL5 configuration, the second-stage blade angle is 24°, exactly half the circumferential angle of the impeller at 48°, while the inter-blade angle of the third stage is staggered by 18° relative to the second. With the first-stage impeller fixed, this configuration produces maximum lift efficiency, a stable internal flow field, and minimal energy exchange loss. As a result, the impellers of multistage pumps should be organised according to the principles presented in this research, which may serve as a guide for future impeller design.

ACKNOWLEDGEMENTS

This work was supported by National Natural Science Foundation of China U24A20140 and U21A20126, Zhejiang Science Foundation Project (Grant No. LY23E060007), Key Research and Development Program of Zhejiang Province (Grant No. 2025C01085), China National Machinery Industry Corporation Technology Project ZDZX2024-11, and Advanced Space Propulsion Laboratory of BICE and Beijing Engineering Research Center of Efficient and Green Aerospace Propulsion Technology (LabASP-2022-02). Also, the authors are grateful for the help provided by Mr. Li of the EBARA GREA PUMPS CO., LTD.

CONFLICT OF INTEREST

The author(s) declared no potential conflicts of interest with respect to the research, authorship, and/or publication of this article.

AUTHORS CONTRIBUTION

Tao Xu: designed the experiment and performed the data analyses. **Baoling Cui:** drafted the manuscript. **LuLu Zhai:** performed the experiments. **ZuChao Zhu:** Revised manuscript.

REFERENCES

Al-Obaidi, A. R. & Alhamid, J. (2024). Analysis of unsteady internal flow characteristics in axial pump with varying number of blades using computational modelling and vibration techniques. *Flow Measurement and Instrumentation*, 99, 102654. https://doi.org/10.1016/j.flowmeasinst.2024.102654

Arnone, A., Marconcini, M., Del Greco, A. S., & Spano, E. (2004). Numerical Investigation of Three-Dimensional Clocking Effects in a Low Pressure Turbine. *Journal of Turbomachinery*, 126(3), 375–384. https://doi.org/10.1115/1.1740780

Barrio, R., Parrondo, J., & Blanco, E. (2010). Numerical analysis of the unsteady flow in the near-tongue region in a volute-type centrifugal pump for different operating points. *Computers & Fluids*, 39(5), 859–870. https://doi.org/10.1016/j.compfluid.2010.01.001

Bohn, D., Ren, J., & Sell, M. (2005). Influence of Stator Clocking on the Unsteady Three-Dimensional Flow in a Two-Stage Turbine. *Journal of Turbomachinery*, 127(1), 156–163. https://doi.org/10.1115/1.1812780

Chen, M. & Tan, L. (2024). Role of particle motion on pressure fluctuation and erosion for a centrifugal pump in energy storage pump station. *Journal of Energy Storage*, 99, 113252. https://doi.org/10.1016/j.est.2024.113252

Chen, W., Li, Y., Liu, Z., & Hong, Y. (2023). Understanding of energy conversion and losses in a centrifugal pump impeller. *Energy*, 263, 125787. https://doi.org/10.1016/j.energy.2022.125787

Fonseca, W. D. P., Perissinotto, R. M., Cerqueira, R. F. L., Verde, W. M., Castro, M. S., & Franklin, E. M. (2024). Particle image velocimetry in the impeller of a centrifugal pump: Relationship between turbulent flow and energy loss. *Flow Measurement and Instrumentation*, 99, 102675. https://doi.org/10.1016/j.flowmeasinst.2024.102675

Ghorani, M. M., Sotoude Haghighi, M. H., Maleki, A., & Riasi, A. (2020). A numerical study on mechanisms of energy dissipation in a pump as turbine (PAT) using entropy generation theory. *Renewable Energy*, 162, 1036–1053. https://doi.org/10.1016/j.renene.2020.08.102

Gu, Y., Pei, J., Yuan, S., Wang, W., Zhang, F., Wang, P., Appiah, D., & Liu, Y. (2019). Clocking effect of vaned diffuser on hydraulic performance of high-power pump by using the numerical flow loss visualization method. *Energy*, 170, 986–997. https://doi.org/10.1016/j.energy.2018.12.204

He, L., Yi, J., Adami, P., & Capone, L. (2015). Space–Time Gradient Method for Unsteady Bladerow Interaction—Part II: Further Validation, Clocking, and Multidisturbance Effect. *Journal of Turbomachinery*, 137(121004). https://doi.org/10.1115/1.4031464

Hongyu, G., Wei, J., Yuchuan, W., Hui, T., Ting, L., & Diyi, C. (2021). Numerical simulation and experimental investigation on the influence of the clocking effect on the hydraulic performance of the centrifugal pump as turbine. *Renewable Energy*, 168, 21–30. https://doi.org/10.1016/j.renene.2020.12.030

Herwig, H. (2010). The Role of Entropy Generation in Momentum and Heat Transfer. *2010 14th International Heat Transfer Conference*, Volume 8, 363–377. https://doi.org/10.1115/IHTC14-23348

Jahani, Z., Khaleghi, H., & Tabejamaat, S. (2022). Using Tip Injection to Stability Enhancement of a Transonic Centrifugal Impeller with Inlet Distortion. *Journal of Applied Fluid Mechanics*, 15(6), 1815–1824. https://doi.org/10.47176/jafm.15.06.1089

Kock, F. & Herwig, H. (2005). Entropy production calculation for turbulent shear flows and their implementation in cfd codes. *International Journal of Heat and Fluid Flow*, 26(4), 672–680. https://doi.org/10.1016/j.ijheatfluidflow.2005.03.005

Luo, Z. Y., Feng, Y., Sun, X. Y., Gong, Y., Lu, J. X., & Zhang, X. W. (2024). Research on the Unsteady Flow and Vortex Characteristics of Cavitation at the Tongue in Centrifugal Pump. *Journal of Applied Fluid Mechanics*, 17(3), 646–657. https://doi.org/10.47176/jafm.17.3.2181

Maestre Di Cioccio, D. O., De Oliveira, W., & Ramirez Camacho, R. G. (2024). Experimental and Numerical Investigation for Predicting the Performance of Voluteless Centrifugal Fan Rotors. *Journal of Applied Fluid Mechanics*, 17(9), 1844–1859. https://doi.org/10.47176/jafm.17.9.2473

Perissinotto, R. M., de Cerqueira, R. F. L., Monte Verde, W., Fonseca, W. D. P., Franklin, E. M., & de Castro, M. S. (2024). Analysis of energy losses and head produced by a radial impeller using particle image velocimetry. *Journal of the Brazilian Society of Mechanical Sciences and Engineering*, 46(9), 576. https://doi.org/10.1007/s40430-024-05117-0

Si, Q., Deng, F., Xu, H., Guo, Y., Ma, W., & Wang, P. (2024). Numerical study on the hydrodynamic characteristics of multi-stage centrifugal pumps influenced by impeller-guide vane clocking effect. *Engineering Applications of Computational Fluid Mechanics*, 18(1), 2351956. https://doi.org/10.1080/19942060.2024.2351956

Tan, M., He, N., Liu, H., Wu, X., & Ding, J. (2016). Experimental test on impeller clocking effect in a multistage centrifugal pump. *Advances in Mechanical Engineering*, 8(4), 1687814016644376. https://doi.org/10.1177/1687814016644376

Walker, G. J. & Oliver, A. R. (1972). The Effect of Interaction Between Wakes From Blade Rows in an Axial Flow Compressor on the Noise Generated by Blade Interaction. *Journal of Engineering for Power*, 94(4), 241–248. https://doi.org/10.1115/1.3445679

Wang, C., Zhang, Y., Zhang, J., & Zhu, J. (2020). Flow pattern recognition inside a rotodynamic multiphase pump via developed entropy production diagnostic model. *Journal of Petroleum Science and Engineering*, 194, 107467. https://doi.org/10.1016/j.petrol.2020.107467

Xu, W., Cheng, L., Lei, S., Yu, L., & Jiao, W. (2024). Mixed-flow pump cavitation characteristics extraction based on power spectrum density through pressure fluctuation signal analysis. *Mechanical Systems and Signal Processing*, 208, 110904. https://doi.org/10.1016/j.ymssp.2023.110904

Yang, C., Zhang, H. Z., Zhao, B., Ma, C. C., & Lao, D. Z. (2015). Analysis of the interaction superposition effect between potential flow and wake in axial compressor blade rows. *Kung Cheng Je Wu Li Hsueh Pao/Journal of Engineering Thermophysics*, 36(2), 269–273.

Zhang, N., Yang, M., Gao, B., Li, Z., & Ni, D. (2015). Investigation of Rotor-Stator Interaction and Flow Unsteadiness in a Low Specific Speed Centrifugal Pump. *Strojniški Vestnik - Journal of Mechanical Engineering*, 62. https://doi.org/10.5545/sv-jme.2015.2859